



HAL
open science

Numerical linear stability analysis of round galactic discs

Christophe Pichon, R. Cannon

► **To cite this version:**

Christophe Pichon, R. Cannon. Numerical linear stability analysis of round galactic discs. Monthly Notices of the Royal Astronomical Society, 1997, 291 (4), pp.616-632. 10.1093/mnras/291.4.616 . hal-04052727

HAL Id: hal-04052727

<https://hal.science/hal-04052727>

Submitted on 31 Mar 2023

HAL is a multi-disciplinary open access archive for the deposit and dissemination of scientific research documents, whether they are published or not. The documents may come from teaching and research institutions in France or abroad, or from public or private research centers.

L'archive ouverte pluridisciplinaire **HAL**, est destinée au dépôt et à la diffusion de documents scientifiques de niveau recherche, publiés ou non, émanant des établissements d'enseignement et de recherche français ou étrangers, des laboratoires publics ou privés.

Numerical linear stability analysis of round galactic discs

C. Pichon^{1,2} and R. C. Cannon^{3,4}

¹*Astronomisches Institut Universitaet Basel, Venusstrasse 7, CH-4102 Binningen, Switzerland*

²*CITA, McLennan Labs, University of Toronto, 60 St George Street, Toronto, Ontario M5S 1A7, Canada*

³*Observatoire de Lyon, 9 Avenue Charles André 69 561 Saint Genis Laval, France*

⁴*University of Southampton, Bassett Crescent East, Southampton SO16 7PX*

Accepted 1997 April 28. Received 1997 April 10; in original form 1996 September 16

ABSTRACT

The method originally developed by Kalnajs for a numerical linear stability analysis of round galactic discs is implemented in the regimes of non-analytic transformations between position space and angle–action space, and of vanishing growth rates. This allows effectively any physically plausible disc to be studied, rather than only those having analytic transformations into angle–action space which have formed the primary focus of attention to date. The transformations are constructed numerically using orbit integrations in real space, and the projections of orbit radial actions on a given potential density basis are Fourier-transformed to obtain a dispersion relation in matrix form. Nyquist diagrams are used to isolate modes growing faster than a given fraction of the typical orbital period, and to assess how much extra mass would be required to reduce the growth rate of the fastest mode below this value. To verify the implementation, the fastest $m = 2$ growth rates of the isochrone and the Kuzmin–Toomre discs are recovered, and the weaker $m = 2$ modes are computed. The evolution of those growth rates as a function of the halo mass is also calculated, and some $m = 1$ modes are derived as illustration. Algorithmic constraints on the scope of the method are assessed, and its application to observed discs is discussed.

Key words: instabilities – methods: analytical – methods: numerical – galaxies: kinematics and dynamics – galaxies: structure.

1 INTRODUCTION

Theoretical studies of the stability of thin stellar discs provide useful constraints on models of galactic formation and dynamics. Disc models can be excluded as unrealistic if they are found to be very unstable, and the results of galaxy formation studies can be clarified where they lead to models close to marginal stability. When applied to observed discs, stability analysis provides a unique tool to probe what fraction of the mass is in luminous form via the requirement that there be enough extra matter to make the observed distribution stable over a period comparable to the age of the galaxy.

Three main approaches have been adopted for disc stability analysis: direct N -body simulations, N -body simulations where the bodies are smeared on to a biorthonormal basis, thereby solving Poisson's equation implicitly, and linear modal analysis. The first has been widely used, initially by Hohl (1971), and more recently by, e.g., Athanassoula & Sellwood (1985). It provides a flexible tool of investigation which can be carried into the non-linear regime. These simulations, however, provide insight into instabilities only in the statistical sense, and generally probe poorly the marginal stability regime. This drawback has recently been addressed by Earn & Sellwood (1995), who developed the second approach of solving Poisson's equation through a biorthonormal basis. The stability of stellar systems has also been explored for spherical systems via a global 'energy principle' (see Sygnet & Kandrup 1984), but this approach has not been successfully implemented for discs because of resonances (Lynden-Bell & Ostriker 1967). Moreover, the method usually provides stability statements which are of little practical use, since no time-scale for the astrophysically relevant growth rates is available.

The third method, linear modal analysis (Kalnajs 1977; Zang 1976; Hunter 1993), is used here. In spite of the obvious limitation to perturbations of small amplitudes, it has several potential advantages. In this approach the integro-differential equation resulting from self-consistent solutions of the Boltzmann and Poisson equations is recast into a non-linear eigenproblem using an appropriately defined orthonormal basis. The method, pioneered by Kalnajs (1971, 1976, 1977) on the linear stability of galactic discs, involves the formulation of the dynamical perturbed equations in angle–action coordinates and the restriction to a (finite) set of perturbed densities which diagonalize Poisson’s equation in position space. Kalnajs’ original work (Kalnajs 1971) concerned the stability of the isochrone disc, for which explicit transformations between angle–action and position–velocity coordinates exist. Zang (1976) studied the self-similar Mestel discs in the same way. More recently, the method was implemented by Hunter (1993) (via repeated evaluation of elliptical integrals) for the infinite Kuzmin–Toomre disc. The approach of these authors involved calculating explicit transformations between angle–action variables and position–velocity variables, and was therefore restricted to a very limited set of simple analytic discs. Also recently, the relevant angle–action integrals were computed by quadrature by Weinberg (1991), and by Bertin (1994) while studying the stability of spherical systems for which the Hamiltonian is separable. Finally, Vauterin & Dejonghe (1996) carried out a similar analysis for discs while performing the whole investigation in position space.

Here, the first step of mapping the distribution function into angle–action space is implemented numerically by calculating the appropriate transformations from the results of integrating unperturbed orbits in the mean field of the galaxy. This then allows considerable freedom in the initial equilibrium to be studied, including the prospect of applying linear stability analysis to distribution functions recovered for observed galaxies. This method is not restricted to integrable potentials, and it could be generalized to three dimensions. It can, in particular, be implemented for *measured* distribution functions, where the potential is deduced from the rotation curve.

In Section 2, Kalnajs’ matrix method is recovered following an indirect route corresponding to a rewriting of Boltzmann’s and Poisson’s equations directly in action space. The stability criteria are then reformulated in a form suitable for numerical evaluation of the matrix elements in Section 3. Details of the numerical method are presented, and its range of validity is discussed. Section 4 contains results of calculations for the isochrone and the Kuzmin–Toomre discs. These are in agreement with those found by Kalnajs (1978), Athanassoula & Sellwood (1985), Hunter (1993) and Earn & Sellwood (1995). Prospects and applications to observed data as probes of dark matter are sketched in Section 5.

2 LINEAR STABILITY ANALYSIS REVISITED

Linear stability analysis concerns the dynamical evolution of initially small perturbations in their own self-consistent field. The derivation (see, e.g., Kalnajs 1977 and Sellwood & Wilkinson 1993) of the resulting integro-differential equation is sketched here, putting the emphasis on a coherent description in action space. This analysis is to be contrasted with that of Vauterin & Dejonghe (1996), who chose to implement stability analysis for discs in position space alone. The resulting dispersion relation, equation (2.17), is fully equivalent to Kalnajs’ equation K-15, but the intermediate integral equation, equation (2.11), also provides a connection with orbital stability analysis (Lynden-Bell 1979; Pichon & Lynden-Bell 1992; Collett 1995).

2.1 The integral equation

The Boltzmann–Vlasov equation,

$$\partial F / \partial t + [H, F] = 0, \quad (2.1)$$

governs the dynamical evolution of an ensemble of collisionless stars. Here H is the Hamiltonian for the motion of one star, F is the mass-weighted distribution function in phase space, and the square bracket denotes the Poisson bracket. Writing $F = F_0 + f$, and $\Psi = \psi_0 + \psi$, where F_0 and ψ_0 are the unperturbed distribution function and potential respectively, and linearizing equation (2.1) in f and ψ , the perturbed distribution function and potential, yields

$$\partial f / \partial t + [H_0, f] - [\psi, F_0] = 0. \quad (2.2)$$

According to Jeans’s theorem, the unperturbed equation, $[H_0, F_0] = 0$, is solved if F_0 is any function only of the specific energy, ε , and the specific angular momentum, h .

Following Lynden-Bell & Kalnajs (1972), angle and action variables of the unperturbed Hamiltonian H_0 are chosen here as canonical coordinates in phase space. The unperturbed Hamilton equations are quite trivial in these variables, which makes them suitable for perturbation theory in order to study quasi-resonant orbits. The actions are defined in terms of the polar coordinates, (R, θ) , by $\mathbf{J} = (J_R, J_\theta)$, where

$$J_R = (2\pi)^{-1} \oint [\dot{R}] dR \quad \text{and} \quad J_\theta = h = R^2 \dot{\theta}. \quad (2.3)$$

Here $[\dot{R}]$ is a function of the radius, R , the specific energy, ε , and the specific angular momentum, h , given by $[\dot{R}] = \sqrt{2\varepsilon + 2\psi_0(R) - h^2/R^2}$. The angle between apocentres is $\Theta = \int h/R^2 [\dot{R}]^{-1} dR$. For a radial period T_R , and a pair of azimuthal and radial epicyclic frequencies Ω and κ , given by $\Omega = \Theta/T_R$ and $\kappa = 2\pi/T_R$ the phase-angles conjugate to J_R and h are $\varphi = (\varphi_R, \varphi_\theta)$, where

$$\varphi_R = \kappa \int^R [\dot{R}]^{-1} dR \quad \text{and} \quad \varphi_\theta = \theta + \int^R (h/R^2 - \Omega) [\dot{R}]^{-1} dR. \quad (2.4)$$

The stationary unperturbed Boltzmann equation (2.1) is solved by any distribution function of the form $F = F_0(\mathbf{J})$, since $[H_0, \mathbf{J}] = 0$.

For growing instabilities, f and ψ are both taken to be proportional to $e^{-i\omega t}$, ω having a positive imaginary part. When expanded in Fourier series with respect to the angles φ , equation (2.2) becomes, after simple algebra (Kalnajs 1977),

$$f_m = \frac{m^{-1} \mathbf{m} \cdot \partial F_0 / \partial \mathbf{J}}{\Omega_\ell - \Omega_p} \psi_m, \quad (2.5)$$

where \mathbf{m} is a integer vector with components (ℓ, m) , $\Omega_\ell = m^{-1} \mathbf{m} \cdot \boldsymbol{\Omega} = \Omega + \ell \kappa / m$, $\boldsymbol{\Omega}$ stands for (κ, Ω) , and $\Omega_p = \omega / m$. Here ψ_m and f_m are the Fourier transforms of ψ and f with respect to $(\varphi_R, \varphi_\theta)$; for instance,

$$\psi_m(\mathbf{J}) = \frac{1}{4\pi^2} \int \psi(R, \theta) \exp[-i(\mathbf{m} \cdot \boldsymbol{\varphi})] d^2\varphi. \quad (2.6)$$

Poisson's integral relates the potential, ψ , to the density perturbation:

$$\psi(R', \theta') = 4\pi G \int \frac{f(\mathbf{R}, \mathbf{v})}{|\mathbf{R} - \mathbf{R}'|} dR d\theta dv_R dv_\theta. \quad (2.7)$$

This equation may be written in order to make explicit the contribution from the interaction of orbits. Here again angle-action variables are useful, as a given unperturbed orbit is entirely specified by its actions. It is therefore straightforward to identify in Poisson's integral the contribution corresponding to the interaction of given orbits. Re-expressing this equation in terms of angles and actions $(\boldsymbol{\varphi}, \mathbf{J})$, using Parseval's theorem and taking its Fourier transform with respect to $\boldsymbol{\varphi}$, leads to

$$\psi_m(\mathbf{J}) = 4\pi G \sum_{\mathbf{m}'} \int f_{\mathbf{m}'}(\mathbf{J}') A_{\mathbf{m}\mathbf{m}'}(\mathbf{J}, \mathbf{J}') d^2\mathbf{J}', \quad (2.8)$$

where ψ_m and f_m are given by equation (2.6), and

$$A_{\mathbf{m}\mathbf{m}'} = \frac{1}{(2\pi)^4} \int \frac{\exp i(\mathbf{m}' \cdot \boldsymbol{\varphi}' - \mathbf{m} \cdot \boldsymbol{\varphi})}{|\mathbf{R} - \mathbf{R}'|} d^2\boldsymbol{\varphi}' d^2\boldsymbol{\varphi}. \quad (2.9)$$

The double sum in equation (2.8) extends in both ℓ and m from minus infinity to infinity, where the radii $\mathbf{R}(\boldsymbol{\varphi}, \mathbf{J})$ and $\mathbf{R}(\boldsymbol{\varphi}', \mathbf{J}')$ are re-expressed as functions of these variables. Now $|\mathbf{R} - \mathbf{R}'|$ depends on φ_θ and φ'_θ in the combination $\varphi'_\theta - \varphi_\theta \equiv \Delta\varphi$ only. As $|\partial(\varphi'_\theta \varphi_\theta) / \partial(\Delta\varphi \varphi_\theta)| = 1$, the order of integration in equation (2.9) may then be reversed, doing the φ_θ integration with $\Delta\varphi$ fixed. This yields $2\pi\delta_{\mathbf{m}\mathbf{m}'}$, so \mathbf{m}' becomes (ℓ', m) in the surviving terms. This gives for equation (2.9)

$$A_{\mathbf{m}\mathbf{m}'} = \frac{2\pi\delta_{\mathbf{m}\mathbf{m}'}}{(2\pi)^4} \int \frac{\exp i(m\Delta\varphi - \ell' \varphi'_R + \ell \varphi_R)}{|\mathbf{R} - \mathbf{R}'|} d\Delta d\varphi'_R d\varphi_R. \quad (2.10)$$

Each m mode therefore evolves independently. The dependence on m will be implicit from now on. So, for example, ψ_ℓ is the Fourier transform of $\psi(R, \theta)$ with respect to both φ_R and φ_θ .

Putting equation (2.5) into equation (2.8) leads to the integral equation

$$\psi_{\ell_1}(\mathbf{J}_1) = 4\pi G \sum_{\ell_2} \int A_{\ell_1 \ell_2}(\mathbf{J}_1, \mathbf{J}_2) \frac{m_2^{-1} \mathbf{m}_2 \cdot \partial F_0 / \partial \mathbf{J}_2}{\Omega_{\ell_2} - \Omega_p} \psi_{\ell_2}(\mathbf{J}_2) d^2\mathbf{J}_2. \quad (2.11)$$

This equation is the integral equation for the linear growing mode with an m -fold symmetry of a thin disc. Equation (2.11) was later approximated by Pichon & Lynden-Bell (1992), Collet (1995) and Lynden-Bell (1994) to analyse the growth of the perturbation in terms of a Landau instability.

2.2 The dispersion relation

The perturbed distribution function and potential are now expanded over a potential-distribution basis $\{f^{(n)}\}_n, \{\psi^{(n)}\}_n$ as

$$f(R, V) = \sum_n a_n f^{(n)}(R, V), \quad \text{and} \quad \psi(R) = \sum_n a_n \psi^{(n)}(R), \quad (2.12)$$

where the basis is assumed to satisfy Poisson's equation (2.7), which when written in action space has Fourier components obeying (following equation 2.8 and given equation 2.10)

$$\psi_{\ell'}^{(n)}(\mathbf{J}) = 4\pi G \sum_{\ell''} \int f_{\ell''}^{(n)}(\mathbf{J}') A_{\ell'\ell''}(\mathbf{J}, \mathbf{J}') d^2 \mathbf{J}'. \quad (2.13)$$

For basis functions scaling like $\exp(im'\theta)$ (preserving the axial symmetry described above), equation (2.6) applied to, say, $\psi^{(n)}(R) \exp(im'\theta)$ gives for the Fourier mode ℓ' :

$$\psi_{\ell'}^{(n)}(\mathbf{J}) = \frac{1}{2\pi} \int_0^{2\pi} e^{-i\ell'\varphi_R} \psi^{(n)}(R[\varphi_R]) e^{im\delta\theta(\varphi_R)} d\varphi_R, \quad (2.14)$$

where equation (2.4) has been used to define the relative azimuthal increment $\delta\theta(\varphi_R) \equiv \varphi_\theta - \theta$.

Expanding ψ over this basis (using the *same* expansion for all ℓ 's) according to equation (2.12), inserting this expansion into equation (2.11), multiplying by $f_{\ell'}^{(p)*}(\mathbf{J})$, integrating over \mathbf{J} , and summing over ℓ' yields

$$\sum_n a_n \left[\sum_{\ell_1} \int \psi_{\ell_1}^{(n)}(\mathbf{J}_1) f_{\ell_1}^{(p)*}(\mathbf{J}_1) d^2 \mathbf{J}_1 \right] = \sum_{n'} a_{n'} \left[4\pi G \sum_{\ell_2, \ell_1} \int \int f_{\ell_1}^{(p)*}(\mathbf{J}_1) A_{\ell_1 \ell_2}(\mathbf{J}_1, \mathbf{J}_2) \frac{m_2^{-1} \mathbf{m}_2 \cdot \partial F_0 / \partial \mathbf{J}_2}{\Omega_{\ell_2} - \Omega_p} \psi_{\ell_2}^{(n')}(\mathbf{J}_2) d^2 \mathbf{J}_2 d^2 \mathbf{J}_1 \right]. \quad (2.15)$$

Since $f_{\ell_1}^{(p)}$ belongs to the basis, it satisfies equation (2.13), and consequently

$$\sum_n a_n \left[\sum_{\ell_1} \int \psi_{\ell_1}^{(n)}(\mathbf{J}_1) f_{\ell_1}^{(p)*}(\mathbf{J}_1) d^2 \mathbf{J}_1 \right] = \sum_{n'} a_{n'} \left[\sum_{\ell_2} \int \psi_{\ell_2}^{(p)*}(\mathbf{J}_2) \frac{m_2^{-1} \mathbf{m}_2 \cdot \partial F_0 / \partial \mathbf{J}_2}{\Omega_{\ell_2} - \Omega_p} \psi_{\ell_2}^{(n')}(\mathbf{J}_2) d^2 \mathbf{J}_2 \right]. \quad (2.16)$$

Requiring that equation (2.16) has non-trivial solutions in $\{a_n\}$ leads to the dispersion relation

$$D(\omega) = \det[\mathbf{\Lambda} - \mathbf{M}(\omega)] = 0, \quad (2.17)$$

where the matrix \mathbf{M} is defined in terms of its components (n', p) by the bracket on the right-hand side of equation (2.16), while the matrix $\mathbf{\Lambda}$ corresponds to the identity if the basis (ψ_n, f_n) is biorthonormal, or to a matrix with components (n, p) by the bracket on the left-hand side of equation (2.16) otherwise. Equation (2.17) was first derived in this context by Kalnajs (1977). In order to approximate the behaviour of a halo, a supplementary parameter $q \in]0, 1]$ is introduced:

$$D_q(\omega) = \det[\mathbf{\Lambda} - q\mathbf{M}(\omega)] = 0, \quad (2.18)$$

as discussed below.

2.3 Unstable modes and Nyquist diagrams

The dispersion relations (2.18) give, for each m , the criterion for the existence of exponentially growing unstable modes of the form $\exp(-i\omega t + im\theta)$. They are functions of a free complex parameter ω corresponding in its real part to m times the pattern speed of the growing mode, Ω_p , and in its imaginary part to the growth rate of the perturbation. The search for the growing modes is greatly facilitated by the use of Nyquist diagrams. Consider the complex ω plane and a contour that traverses along the real axis and then closes around the circle at ∞ with $\text{Im}(\omega)$ positive. The determinant D_q is a continuous function of the complex variable ω ; so, as ω traces out the closed contour, $D_q(\omega)$ traces a closed contour in the complex D_q plane. If the $D_q(\omega)$ contour encircles the origin, then there is a zero of the determinant inside the original contour, and the system is unstable. In fact, a simple argument of complex analysis shows that the number of loops around the origin corresponds to the number of poles above the line $\text{Im}(\omega) \equiv \eta = \text{constant}$. An intuitive picture of how the criterion operates on equation (2.17) is provided by the following thought experiment. Imagine turning up the strength of qG for the disc (i.e., turn on self-gravity, which is

physically equivalent to allowing for the gravitational interaction to play its role; alternatively, vary q , the ratio of relative halo support). Starting with small qG , all the M^{mp} are small, so for all ω s the determinant $D_q(\omega)$ remains on a small contour close to $\det|\Lambda|$. As qG is increased to its full value, either the D_q contour passes through the origin to give a marginal instability or it does not. If it does not, then continuous change of qG does not modify the stability, and therefore the self-gravitating system has the same stability as in the zero qG case: it is stable. If, however, it crosses, and remains circling the origin, then it has passed beyond the marginally stable case and is unstable. This picture is illustrated in the next sections, where the image of the complex line $m\Omega_p + i\eta$, $\Omega_p \in]-\infty, \infty[$, is plotted for various values of η .

3 NUMERICAL IMPLEMENTATION

3.1 Method

Stability analysis, as implemented in the previous section, allows the treatment of a wide range of potentials and distribution functions which, in general, will not afford the explicit transformations between angle–action variables and velocity–position variables.

Spline interpolation for tabulated potentials and distribution functions is used to compute the transformation of variables by numerically integrating orbits in the given potential. The whole calculation is performed on a grid of points in (R_0, V_0) space, where R_0 is the radius at apocentre, and V_0 is the corresponding tangential velocity. As may be seen from Fig. 4 in Section 3.2, a 40×40 grid is adequate for the discs considered here.

For each point in this grid, three orbits are calculated, one starting at the grid-point itself, and the others at small deviations in $h_0 = R_0 V_0$, and along $h_0 = \text{constant}$. The angles and actions for these orbits are used later to calculate numerical derivatives of the distribution function. A fourth-order Runge–Kutta integration scheme is employed for the orbits, stopping at the first pericentre for all but the most eccentric orbits where more than one oscillation is needed to give sufficient accuracy in the actions. Further points on the orbits corresponding to grid vertices are then calculated at exact subintervals of the orbital period. The Fourier components ψ_l^n of a particular basis element along an orbit equation (2.14) are then given by

$$\psi_l^{(n)}(R_0, V_0) = \frac{1}{T_R} \int_0^{T_R} e^{-2\pi i l t / T_R} \psi^{(n)}(R[t]) e^{i m \delta \theta(t)} dt, \quad (3.1)$$

where $t = \varphi_R / \kappa$, and

$$\delta \theta(\varphi_R) = \kappa^{-1} \int^{\varphi_R} \frac{h}{5R^2} d\varphi_R - \kappa^{-1} \frac{\varphi_R}{2\pi} \oint \frac{h}{R^2} d\varphi_R = \theta(t) - \langle \dot{\theta}(t) \rangle t. \quad (3.2)$$

Numerically, this simply corresponds to taking a discrete Fourier transform (DFT) over the resampled points. The symmetry of an orbit means that although the argument is complex, the result is purely real.

The matrix element defined in equation (2.16) is rewritten in terms of (R_0, V_0) and truncated in ℓ :

$$M^{(n)(n')}(\omega) = \sum_{\ell=-L}^{\ell=L} \int \int \psi_l^{(n)*} \frac{(\partial F / \partial h \cdot m + \partial F / \partial J \cdot \ell)}{\Omega \cdot m + \kappa \cdot \ell - m\Omega_p - i\eta} \psi_l^{(n')} \left| \frac{\partial J \partial h}{\partial R_0 \partial V_0} \right| dR_0 dV_0, \quad (3.3)$$

where the $\psi_l^{(n)}$ are now surfaces in (R_0, V_0) space given by the ℓ th-order term of the DFT of the orbit at R_0, V_0 .

The inclusion of retrograde stars may be effected transparently by specifying a grid in R_0, V_0 which includes negative V_0 or, more efficiently, by noting that

$$\psi_l^{(n)}(-h) = \frac{1}{\pi} \int_0^\pi \cos[\ell \varphi_R(-h) - m \delta \varphi(-h)] \psi^{(n)}\{R[\varphi_R(-h)]\} d\varphi_R, \quad (3.4a)$$

$$= \frac{1}{\pi} \int_0^\pi \cos[\ell \varphi_R(h) + m \delta \varphi(h)] c^{(n)}\{R[\varphi_R(h)]\} d\varphi_R, \quad (3.4b)$$

$$= \psi_{-l}^{(n)}(h); \quad (3.4c)$$

so, with the appropriate sign switching, the same set of orbits and Fourier modes may be used as for prograde stars.

Having calculated the derivatives of the distribution function with respect to J and h by finite differences across the slightly displaced orbits described earlier and the Jacobian $\partial(Jh)/\partial(R_0 V_0)$ in the same manner, the problem of computing the matrix elements of equation (3.3) reduces to one of integrating quotients of surfaces on the R_0, V_0 grid. It is worth noting that, although it is the steps of the calculation up to this point which provide the generality of the implementation, their

computational cost is relatively slight, amounting in total, for example, to about 1 min on a workstation with a specFp92 of 100.

For vanishing growth rates, the integrand in equation (3.3) is a quotient of surfaces with a real numerator but a denominator which may vanish along a line within the region of integration. The integral then exists only as a principal-value integral. Rather than attempting a brute-force discretization, we approximate both numerator and denominator by continuous piecewise flat surfaces and employ analytic formulae, or their power-series expansions, for each flat subsection. Each square of the R_0, V_0 grid is treated as two triangles. According to the magnitudes and slopes of the two surfaces over a given triangle there are six different approximations to be used for each component of the integral. For modes with finite growth rates, the integrand in equation (3.3) is of a quotient of surfaces with a real numerator but a complex denominator, and this prescription still holds. The extra generality afforded yields a solution which handles transparently the marginal stability case, where the resonances can be infinitely sharp.

The integration and summation then yields, for each Ω_p and η , an $n \times n$ matrix \mathbf{M} . Marginal stability corresponds to the vanishing of $\det|\mathbf{I} - \mathbf{M}|$. As described in Section 2.3, it is convenient to use Nyquist diagrams to locate the critical points: matrices corresponding to about 100 values of ω are calculated for lines of constant η . Provided that the sampling is good enough, the number of times the line $\det|\mathbf{I} - \mathbf{M}|$ encircles the origin in the complex plane gives the number of zeros above the initial line $m\Omega_p + i\eta$. An example of Nyquist diagrams for the isochrone/9 disc (Section 4) is illustrated in Fig. 1 and shown more quantitatively in Figs 2 and 3. The three-dots-dashed curve corresponds to $\eta = 0.16$ and does not encircle the origin (or rather it loops once clockwise and once anticlockwise), whereas the other two curves ($\eta = 0.12$ and 0.14) do, indicating that the growth rate for the fastest growing bisymmetric instability of this disc is between 0.14 and 0.16.

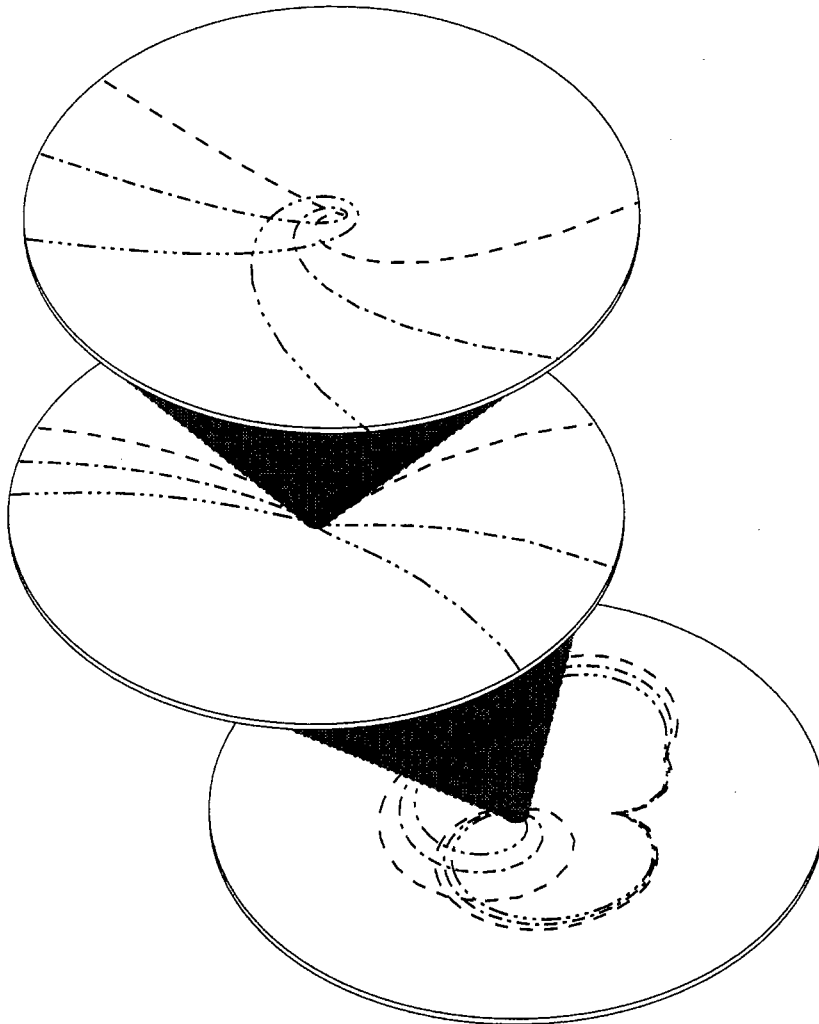


Figure 1. Nyquist diagram for the fastest growing mode of an isochrone/9 model for growth rates $\eta = 0.12$ (dashed curve), $\eta = 0.14$ (dot-dashed curve) and $\eta = 0.16$ (dot-long-dashed curve). The magnification shows that the first two curves do enclose the origin, whereas the third does not, indicating that the true growth rate is between 0.14 and 0.16.

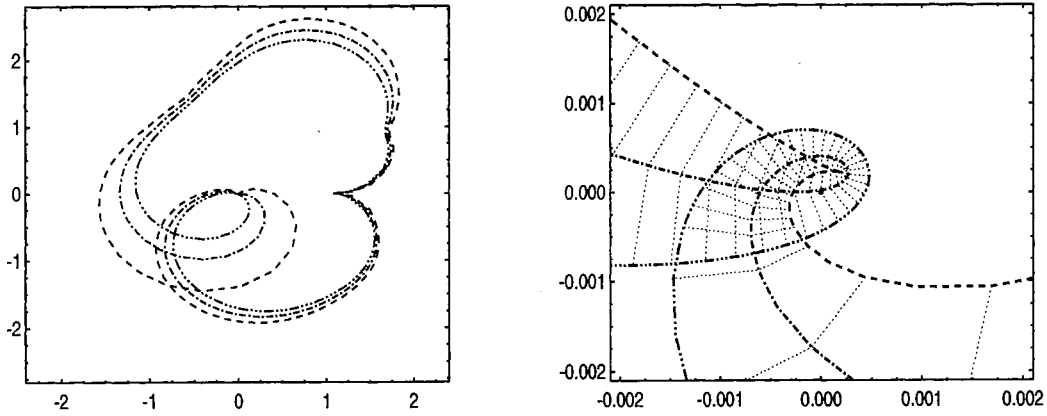


Figure 2. Nyquist diagram for the fastest growing mode of an isochrone/9 disc with curves labelled as in Fig. 1. The dotted lines join points for the same ω .

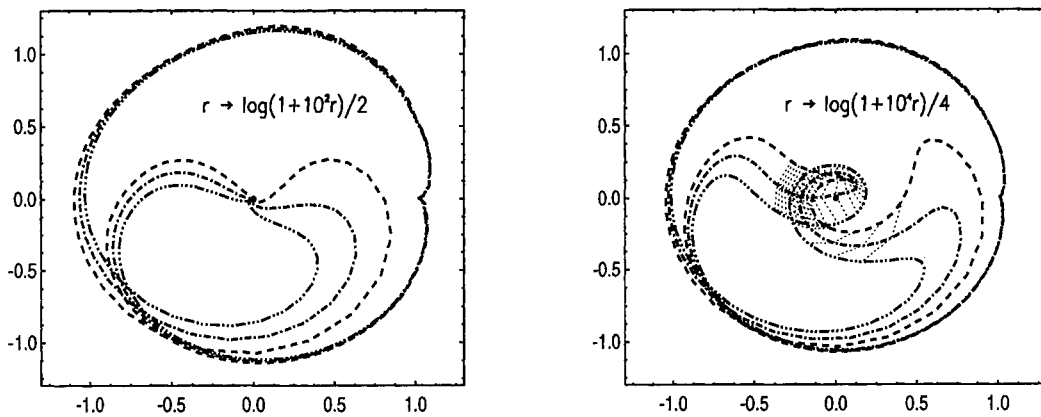


Figure 3. Nyquist diagram for the fastest growing mode of an isochrone/9 as in Figs 1 and 2. A logarithmic scaling has been applied near the origin mapping $r \rightarrow \log_{10}(1 + 10^r)/\alpha$, allowing the full topology to be seen more easily.

This method is easy to apply to verify calculations where the growth rate and pattern speed are already known, but becomes more time-consuming when treating discs with unknown properties. Many automatic schemes can be envisaged for locating zeros in the complex plane but, since computing the matrices is the slowest part of the calculation, we have found it most efficient to manage the search by hand with an interactive tool for examining Nyquist diagrams for different values of q (Section 2.3). With a little experience, the zeros can be efficiently located even from poorly sampled diagrams with spurious loops which would easily lead to confusion in automated procedures.

3.2 Validation

There are two distinct types of errors to be assessed in this analysis: numerical errors arising from the discretization of integrals and from machine rounding, and truncation errors relating to the use of small finite bases, limited Fourier expansions and the calculation of only the inner parts of infinite discs.

While, in principle, constraining the first type of errors is purely routine, it is worth noting that both the bases considered here require the use of arbitrary precision languages (such as `bc`) for their evaluation. As noted by Earn & Sellwood (1995), Kalnajs' basis requires the use of about 50 figures precision to get the first 30 basis elements to five figures. The problem, however, lies only in evaluating the polynomial terms, because the coefficients are large and induce substantial cancellations. Qian's basis (1992) not only requires extended precision to evaluate a single element, but it is also extremely close to being singular.

Besides evaluation of the basis elements, the only other part requiring special care is in the numerical derivatives of the distribution function with respect to J and h , where a tight compromise must be made between the desire for a small interval to give an accurate derivative, and the loss of significance in the differences between angles and actions calculated for very close orbits. Nevertheless, a straightforward Runge–Kutta scheme for the orbits remains adequate in all the cases studied here.

The second class of errors – those arising from the truncation of equations (2.17) – are best assessed by simply recomputing the same quantity with more basis functions, more Fourier harmonics, or a larger disc. The results of these tests for all the truncated quantities can be seen in Figs 4 and 5. All these results are for the isochrone/9 model first studied by Kalnajs (1976) with the $n=7$ series of Kalnajs' basis functions, which is further discussed in Section 4. Since the calculation of the matrix $\mathbf{M}(\omega)$ in equation (2.18) is the most computationally intensive operation, the self-gravity parameter q is taken instead of the growth rate η as a convergence criterion. The q plotted in the figures is that which satisfies equation (2.18). It is found by bisection with respect to the winding number of the Nyquist diagram. A value $q=1$ for the expected exact growth rate (given by Kalnajs 1978) is the asymptote towards which the calculation should converge when the appropriate range of parameters have been found.

Fig. 4 shows how the sampling affects the result when the initial R_0, V_0 grid has the same number of points in each direction. The different lines in this and subsequent figures indicate how q converges for different sizes of basis. The figure shows that for this disc, a sampling with a 40×40 grid reduces the sampling errors well below those from the basis truncation. The right-hand panel shows how the truncation of the disc influences convergence for different sizes of basis. If the instability is localized to the inner parts of the disc, including more of the outer regions should not affect the result. The behaviour seen here is due to stretching of the basis when R_{\max} is increased, so more functions are required to sample the inner regions to the same resolution. If, however, enough functions are used, no change is seen beyond about $R_{\max}=4.5$.

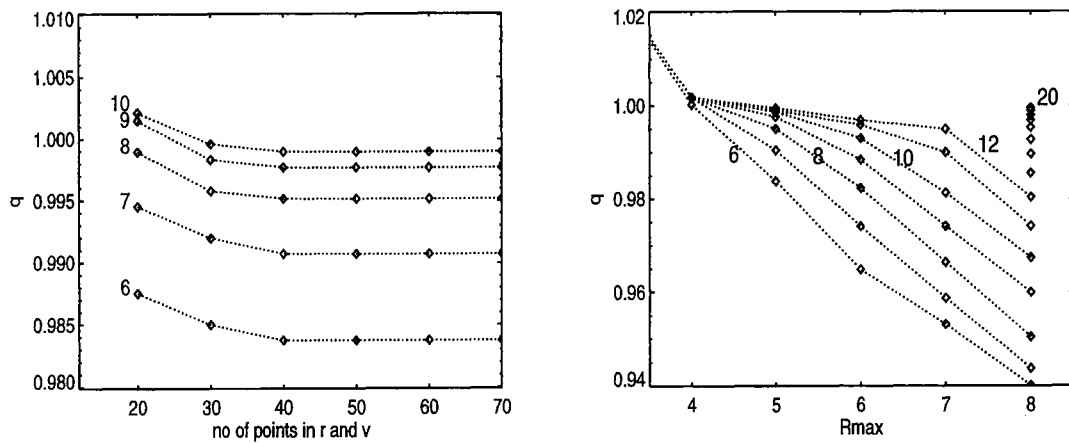


Figure 4. The self-gravity parameter, q , as a function of the grid sampling, and the disc truncation. Data are shown for bases of various sizes as labelled. In the right-hand panel, q is shown as a function of the truncation radius of the disc for different sizes of basis as labelled. More functions are needed for convergence with larger R , because the inner, dominant, part of the disc is less well sampled when the basis is stretched over a larger domain. As with all the figures in this section, the disc is Kalnajs' isochrone/9 model. The basis is Kalnajs' biorthonormal set with $k=7$.

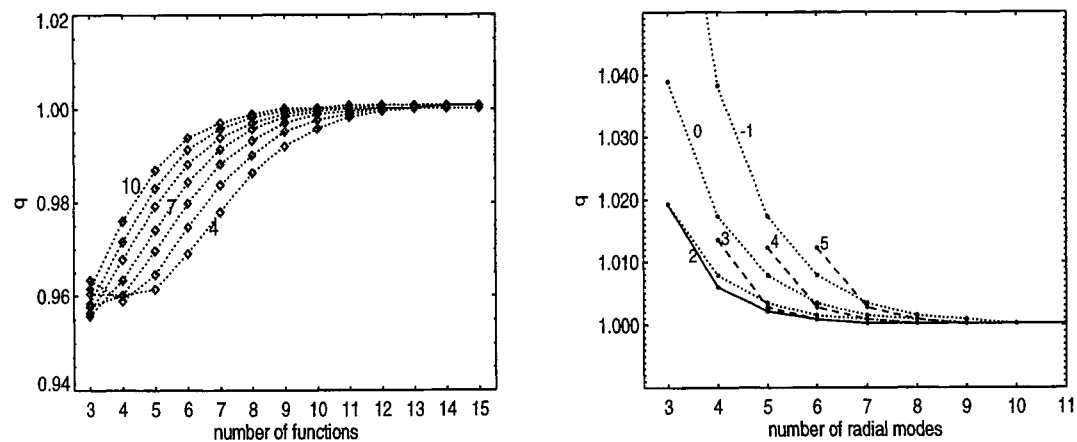


Figure 5. The dependence of the self-gravity parameter, q , upon the order of the basis, the number of functions used in the calculation, and the number of radial harmonics. The left-hand panel shows q against the basis size for different bases from Kalnajs' set, labelled by the corresponding k parameter. In the right-hand panel, 12 functions were used, with the number of radial harmonics on the abscissa taken on either side of a central value as labelled on the lines. Centring the harmonics on 2 (when looking for bisymmetric instabilities) shows appreciably better convergence than taking equal numbers of positive and negative harmonics (centre 0).

As remarked by Earn & Sellwood (1995), choosing an appropriate basis for a given instability has a significant effect on the number of basis functions necessary to resolve the mode. This may be seen in Fig. 5 for Kalnajs' set of biorthonormal bases with $4 \leq k \leq 10$. 10 functions with the $k=4$ basis are required to give the same error in q as achieved with only six functions in the $k=10$ basis. Kalnajs remarks that some economies may be made by not using the same number of positive and negative radial Fourier modes but by centring the range on m , the order of the instability. This is illustrated in the right-hand panel, where the abscissa gives the number of radial modes on each side of a central value as labelled. The computational load is almost directly proportional to the number of radial modes to be used, so this effect is well worth exploiting. Developing a specific basis for different thin discs also speeds up the calculation, by reducing the number of functions required for convergence, but it is not necessary. Any reasonable basis will get there in the end, and the feasibility of the resulting computations considerably enhances the generality of this approach. Finally, Fig. 6 illustrates the convergence of the shape of the mode as a function of the number of basis functions.

4 APPLICATION: THE ISOCHRONE AND KUZMIN-TOOMRE DISCS

The versatility of the algorithm for linear stability described above is now illustrated while recovering growth rates and pattern speeds of previously studied discs with old and new distribution functions, finding the modal response – in position space and in action space – of these discs both for bisymmetric and lopsided modes.

4.1 The equilibria

Three families of discs are studied here: two corresponding to equilibria for the isochrone disc (Hénon 1961), and one for the Kuzmin–Toomre mass model (Kuzmin 1956). The isochrone disc is defined by its potential, $\psi = GM/(b + r_b)$, where $r_b^2 = R^2 + b^2$. The corresponding surface density is $\Sigma = Mb \{ \ln[(R + r_b)/b] - R/r_b \} / (2\pi R^3)$. The Kuzmin–Toomre potential is defined by $\psi = GM/r_b$, and the corresponding surface density is $\Sigma = Mb/2\pi r_b^3$. Miyamoto (1974), followed by Kalnajs (1976), Athanassoula & Sellwood (1985) and Pichon & Lynden-Bell (1996), chose specific forms of distribution functions, assuming simple algebraic Ansatz for its expression in (ε, h) space. Historically, these models were first used to construct families of maximally rotating discs (e.g., the Miyamoto/ m_M disc models – Hunter 1993), while for others, counter-rotating stars were re-introduced by simple, though somewhat arbitrary, tricks (Kalnajs 1978) described by Earn & Sellwood (1995). In this paper, the Kalnajs isochrone/ m_K models are implemented in order to recover Kalnajs' (1978) first linear stability results on differentially rotating discs. To demonstrate the flexibility of the method, the truncated version of Hunter's Kuzmin–Toomre/ m_M models is also constructed, and the stability of the equilibria given by Pichon & Lynden-Bell (1996) is analysed.

Kalnajs' distribution family reads (in units of b and $G=1$)

$$f_K(\varepsilon, h) = 2^{2m-1} (\sqrt{-2\varepsilon h})^{-m} \pi^{-1} (-\varepsilon)^{m-1} g(\sqrt{-2\varepsilon h}), \quad (4.1)$$

where

$$g(x) = x \frac{\partial [x^m \tau_m(x)]}{\partial x} + \int_0^1 (tx)^m \tau_m(tx) P_{m-1}''(t) dt - \frac{1}{2}(m-1)mx^m \tau_m(x), \quad (4.2)$$

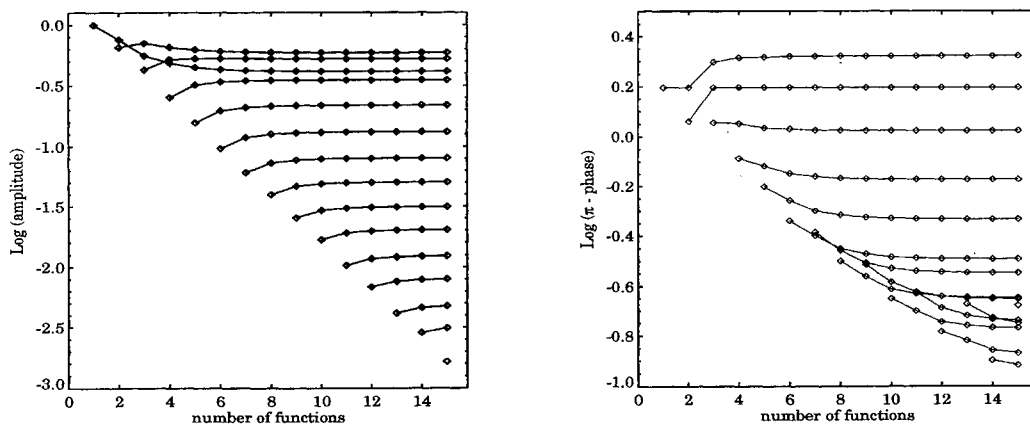


Figure 6. The amplitude (left-hand panel) and the phase (right-hand panel) of components of the critical eigenvectors as a function of the number of basis functions. The rapid convergence of the shape of the mode appears clearly.

and

$$\tau_m(x) = \frac{\log(r + \sqrt{1+r^2}) - r/\sqrt{1+r^2}}{2\pi r^3(-1 - \sqrt{1+r^2})^{-m}} \Big|_{r=2x/(x^2-1)} \quad (4.3)$$

Here P_m stands for the Legendre polynomial of order m . Pichon & Lynden-Bell's distribution family for the isochrone disc is given by

$$f_P(\varepsilon, h) = \frac{(-\varepsilon)^{m+1/2}}{4\pi^2(m+1/2)!!} \frac{h}{\sqrt{2}} \left(\frac{\partial}{\partial s} \right)^{m+2} [(s^2-1)_m L(s)] \Big|_{s=1+h^2/2}, \quad (4.4)$$

with $L(s) = \log(\sqrt{s^2-1} + s) + \sqrt{s^2-1}/s$. Its contours for $m_p=4$ are illustrated in Fig. 7, while the Q profiles are given by Pichon & Lynden-Bell (1996, fig. 5). Finally, Miyamoto's distribution is

$$f_M(\varepsilon, h) = \frac{(2m+3)}{2\pi^2} (-\varepsilon)^{2+2m} {}_2F_1\left(-m, -2-2m, \frac{1}{2}, \frac{-h^2}{2\varepsilon}\right), \quad (4.5)$$

where ${}_2F_1$ is a terminating hypergeometric function of the second kind.

4.2 Characteristics of the linear wave

4.2.1 Bisymmetric $m=2$ modes

The pitch angle of the spiral response is commonly defined as $\cot(i) = \langle \partial\theta/\partial \log(R) \rangle_\theta$, where $\theta = \theta(R)$ at the crest of the spiral wave. In practice, it is best to calculate $\tan(i) = \langle \partial \log(R)/\partial \theta \rangle_R$ since $R=R(\theta)$ is a bijection in $[0, 2\pi/m[$. Another useful set of quantities are defined by the radius, $R_{1/2}$, (resp. the angle $\theta_{1/2}$) at which the spiral response has decreased to half its maximum amplitude. The winding number $n_{1/2} = \theta_{1/2}/(2\pi)$ yields a measure of the winding of the wave: the larger $n_{1/2}$ is, the more wound it is. Comparing the position of the resonances and R_{\max} to $R_{1/2}$ provides the means to assess whether the truncation of the disc is likely to have generated spurious cavity waves. Specifically, it is required that $R_{1/2} < R_{\text{OLR}} < R_{\max}$, so that the wave is well damped by the outer Lindblad resonance before the disc is truncated. Numerical simulations have suggested that $R_{1/2} \sim R_{\text{COR}}$. Both statements are verified here for instance in Fig. 10 (resp. Fig. 11), which gives the linear response of a $m_k=7$ and a $m_k=11$ isochrone disc (resp. $m_k=5$ Kuzmin disc) for its first growing mode. These perturbations display the usual bar-shaped

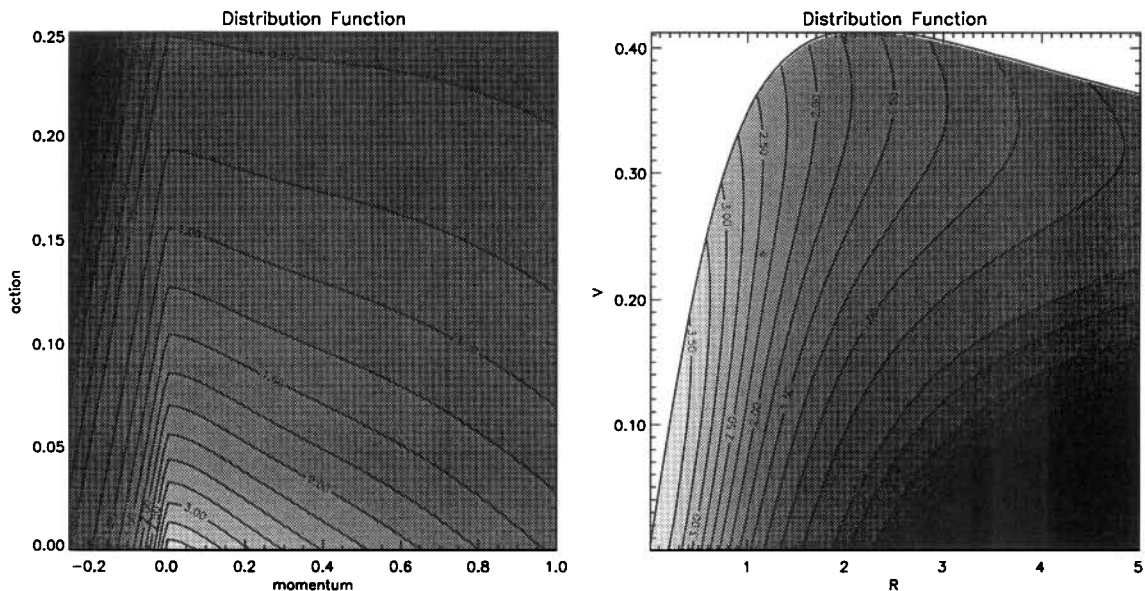


Figure 7. Left-hand panel: isocontours of the $m_p=4$ distribution function in action space. The sharp break at zero momentum is an artefact of Kalnajs' trick which was used here to incorporate counter-rotating stars; right-hand panel: same isocontours for the prograde stars only in (R_0, V_0) – apocentre, velocity at apocentre – space. These variables are those used throughout the calculation to label the orbits. Note the envelope corresponding to the rotation curve of that galaxy. It appears clearly in this parametrization that in this galaxy most orbits are of low ellipticity.

central response with a loosely wound spiral response further out. Fig. 12 gives the evolution of $\cot(i)$, $R_{1/2}$, $n_{1/2}$, Ω_p and η as a function of the Toomre number Q of the Kalnajs $/m_K$ discs. Tables 1–3 give the growth rates and pattern speeds of the $/m_K$, $/m_P$ and $/m_M$ families. Note that for the new $/m_P$ family the bar modes given in Table 2 again have pattern speeds well above the maximum of $\Omega - \kappa/2$, and hence do not display inner Lindblad resonance. Note also that the more compact Kuzmin–Toomre potential has larger growth rates and pattern speeds, as expected since the dynamical time is shorter and the self-gravity is enhanced for those discs. Table 4 gives the growth rates for the second and the third growth rate of the m_K discs. Note that the growth rate of the second fastest growing mode of a $m_K=12$ model was found by this method to equal $\omega + i\eta = 0.461 + 0.145i$, roughly within the error bars given by Earn & Sellwood (1995). Note that the number of radial nodes for these slower modes increase with the rank in stability (as illustrated in Fig. 16 for an $m=1$ mode discussed in the next subsection), which is consistent in so far as winding decreases self-gravity. Note also the small relative error between the growth rates recovered for the Myamoto/Hunter models and those given by Hunter (1993) for the Kuzmin–Toomre discs. Small residual discrepancies are expected, given that Hunter’s discs are infinite, whereas those studied here are truncated at $R=5$. Fig. 8 gives for the m_K and m_P families the evolution of the first growing mode as a function of the Toomre Q number (mass-averaged in the inner region $R < 2$) of these discs and ‘the mass in the halo’ as parametrized by q . An *new* attempted fit of a combination of Q and q is also given in Fig. 9 for both distributions; the relative dispersion illustrates the well-known

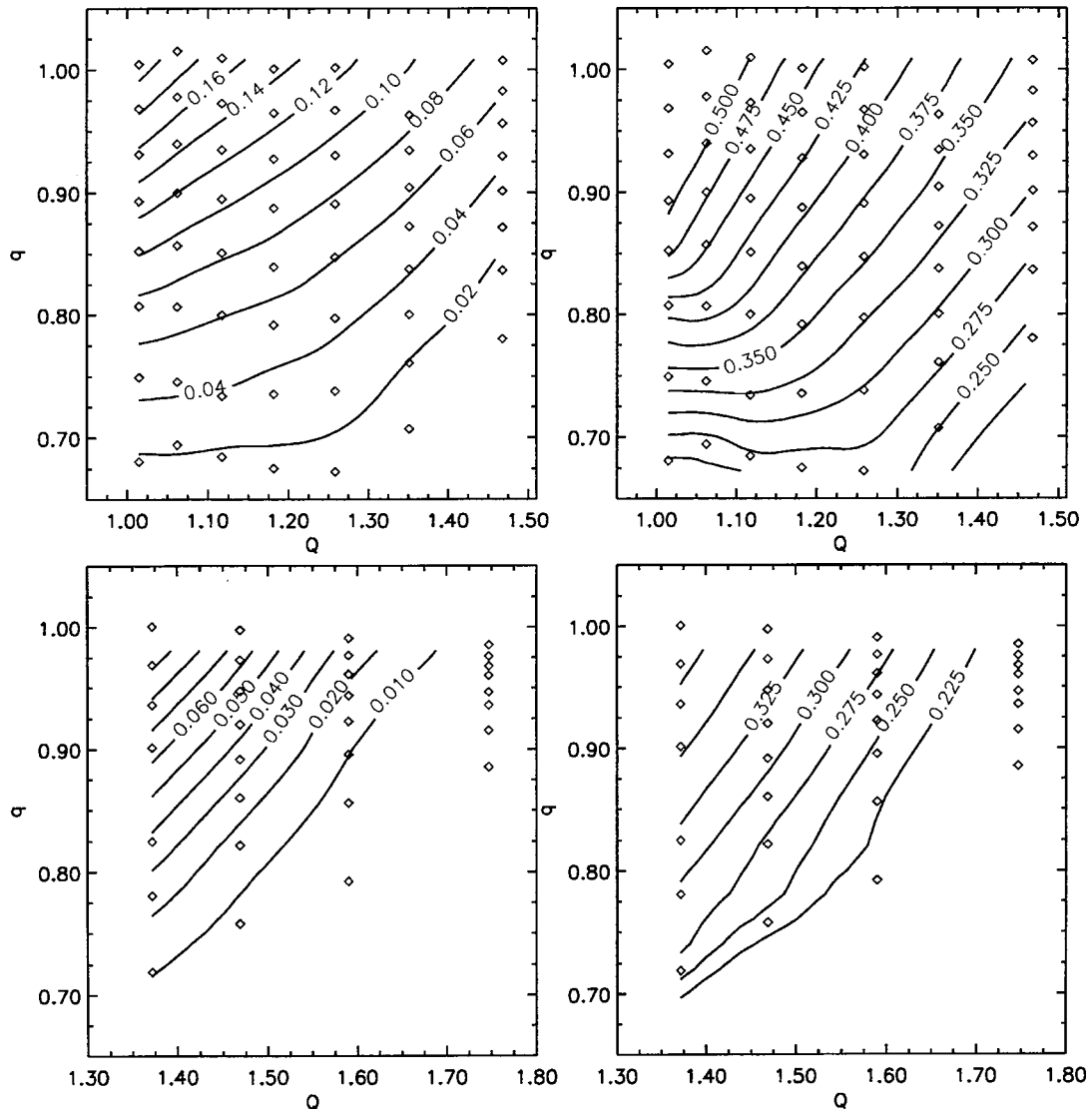


Figure 8. The variation of the $m=2$ growth-rate (top-left panel) and the pattern speed (top-right panel) of an isochrone/ m_K family as a function of the self-gravity parameter q and the Toomre number Q . The bottom panels show the same results for the isochrone/ m_P family. The precision in the growth-rates – at fixed truncation in the basis – drops for lower values of Q , since these modes are more centrally concentrated.

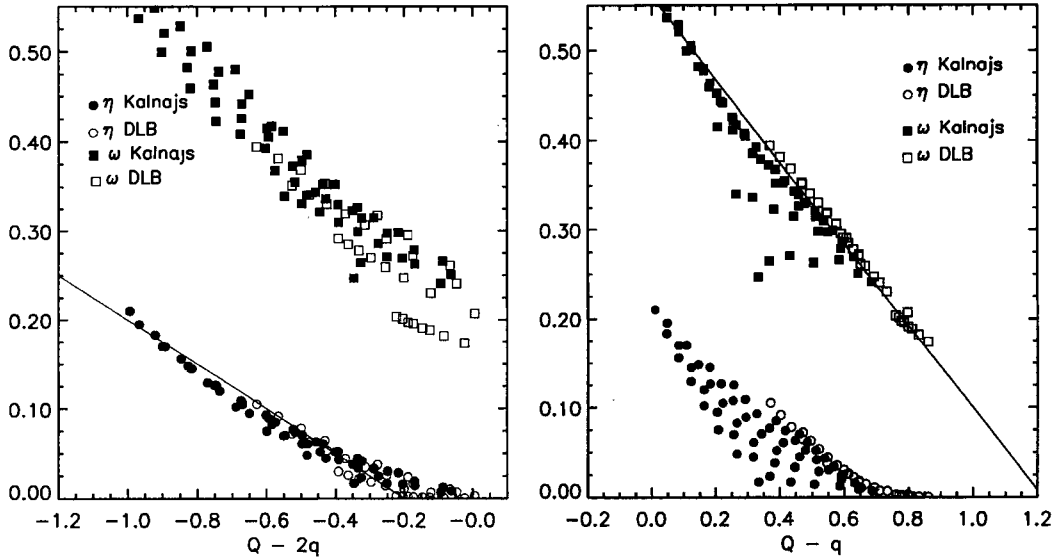


Figure 9. Fits to the evolution of the $m=2$ growth rate and the pattern speed of an isochrone/ m_K (marked Kalnajs) and an isochrone/ m_p (marked DLB) family as a function of a linear combination of the self-gravity parameter q and the Toomre number Q . The left-hand panel minimizes the dispersion in η , whereas the right-hand panel minimizes that in ω . The best fits are obtained for different linear combinations of Q and q . The solid line for η is $\eta = -0.05 - 0.25(Q\zeta q)$ and that for ω : $\omega = 0.56 - 0.46(Q - q)$.

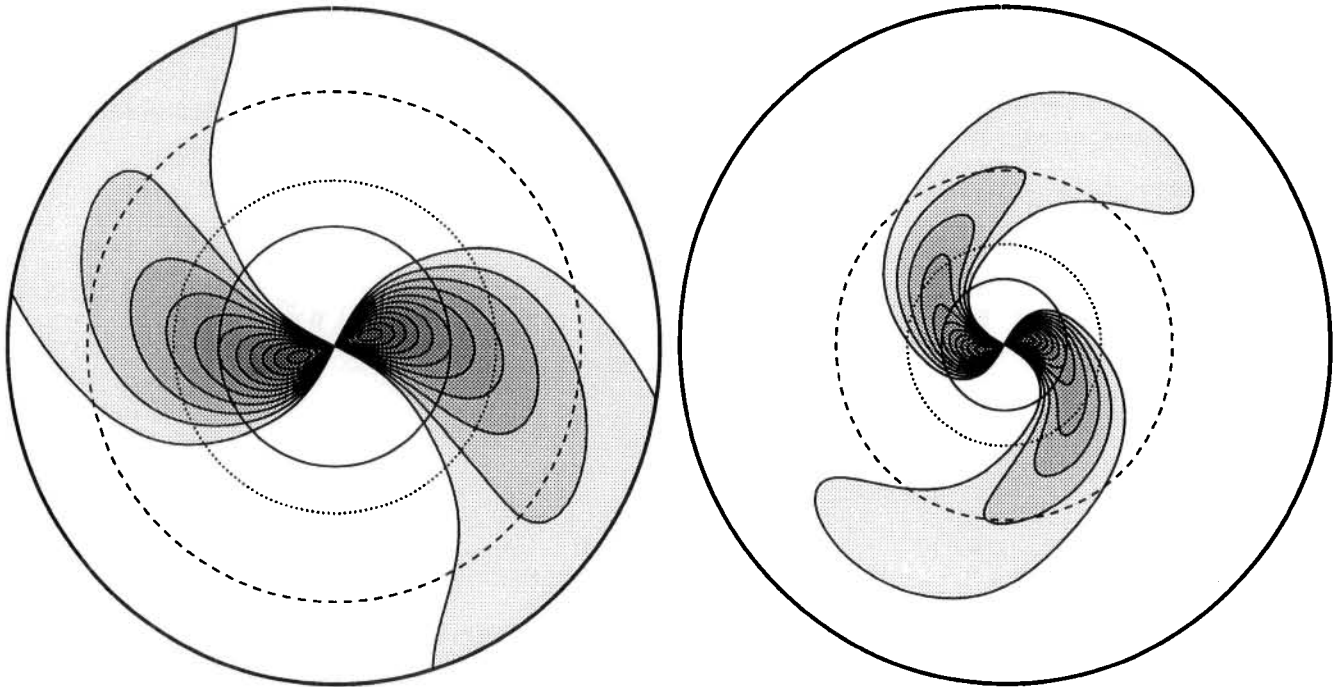


Figure 10. The density response corresponding to the fastest $m=2$ growing mode of the isochrone/7 and isochrone/11 model. Note that the colder /11 model yields a more tightly wound spiral, as shown quantitatively in Fig. 12. This is expected, since in the locally marginally radially unstable regime, the disc response should asymptotically match that of unstable rings. Its spiral response is also more centrally concentrated than that of its hotter counterpart. The solid circle corresponds to $R_{1/2}$, the radius at which the wave has damped by a factor of 2, the dotted circle to corotation resonance, the dashed circle to the outer Lindblad resonance, and the outer circle to $R_{\max} = 5$.

fact that the stability does not depend only on a simple combination of these numbers. These curves seem to be in qualitative agreement with those given by Vauterin & Dejonghe (1996) for different disc models. Here, too, the pattern speed at fixed growth rate is a decreasing function of the Q number ($\partial\Omega_p/\partial Q_\eta < 0$). The conjecture of Athanassoula & Sellwood (1985) of an asymptotic value of $Q \approx 2$ for marginal stability of *fully self-gravitating discs* seems also consistent with these results.

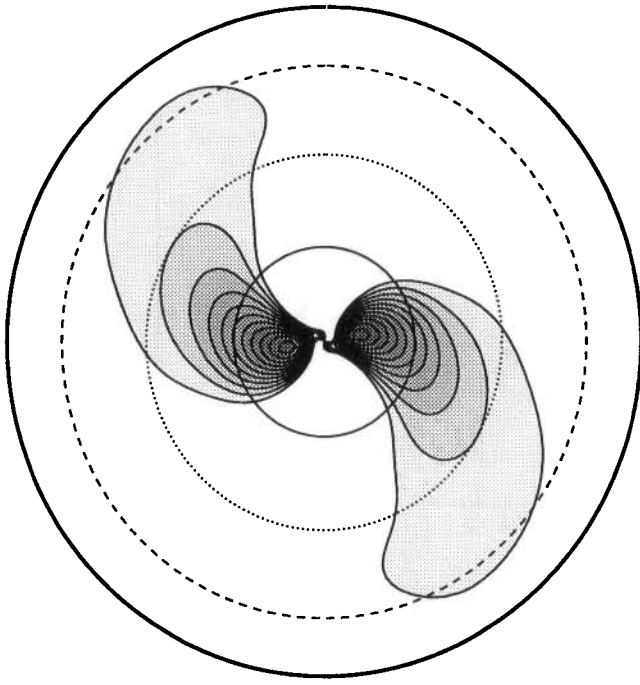


Figure 11. Same as Fig. 10 for a Myamoto–Hunter/3 model. Note that the response is much more centrally concentrated, since the outer circle is $R_{\max}=3$. This is expected, since the Kuzmin–Toomre potential is more compact than the isochrone.

Table 1. $m=2$ growth rates and pattern speed of the isochrone/ m_K model.

The isochrone/ m_K model: bisymmetric mode

Model	$m\Omega_p$	η
6	0.34	0.075
7	0.37	0.085
8	0.43	0.125
9	0.47	0.145
10	0.50	0.170
11	0.53	0.195
12	0.59	0.210

Table 3. $m=2$ growth rates and pattern speed of the Toomre/ m_M model.

The Toomre/ m_M model: bisymmetric mode

Model	$m\Omega_p$	η
2	0.598	0.204
3	0.714	0.294
4	0.810	0.371
5	0.916	0.445

4.2.2 Lopsided $m=1$ modes

The algorithm presented in Section 3 is, in principle, inadequate to address the growth of $m=1$ perturbations which for purely self-gravitating discs are forbidden, since the perturbation does not conserve momentum. Following Zang (1976), it is assumed here that the disc is embedded in some sufficiently massive halo to compensate its infinitesimal centre of mass shift. Fig. 15 gives the $m=1$ modal response of the isochrone/ $m_{10,11}$ discs, while the corresponding pattern speeds and growth rates are given

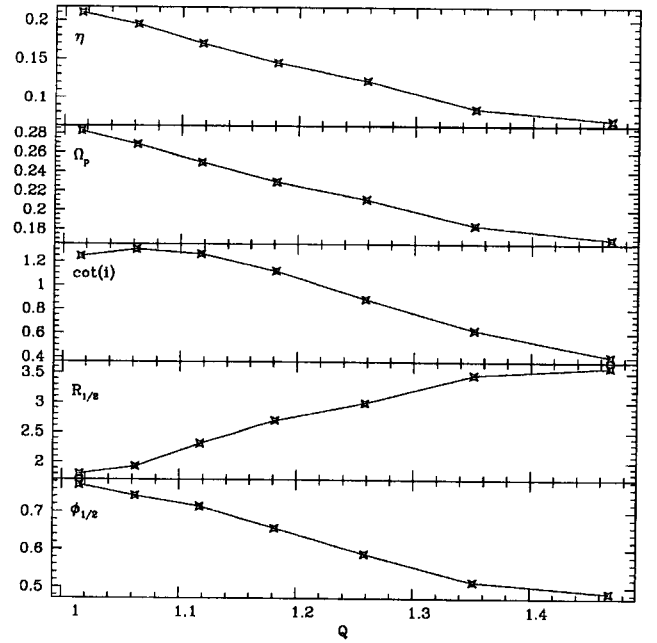


Figure 12. The evolution of η , Ω_p , $\cot(i)$, $R_{1/2}$ and $n_{1/2}$, as a function of the Toomre number Q of the isochrone/ m_K discs. Note that the hotter disc have less wound spiral response.

Table 2. $m=2$ growth rates and pattern speed of the isochrone/ m_p model.

The isochrone/ m_p model: bisymmetric mode

Model	$m\Omega_p$	η
3	0.21	0.003
4	0.29	0.032
5	0.35	0.072
6	0.40	0.105

Table 4. Second and third fastest $m=2$ growing modes of the isochrone/ m_K model.

The isochrone/ m_K model: bisymmetric mode

Model	Second mode	Third mode
7		
10	$0.29(4) + 0.04(1)i$	$0.22(0) + 0.008(8)i$
11	$0.39(7) + 0.10(5)i$	$0.27(3) + 0.039(5)i$
12	$0.42(8) + 0.12(8)i$	$0.34(7) + 0.091(5)i$
	$0.46(1) + 0.14(5)i$	$0.26(4) + 0.051(2)i$

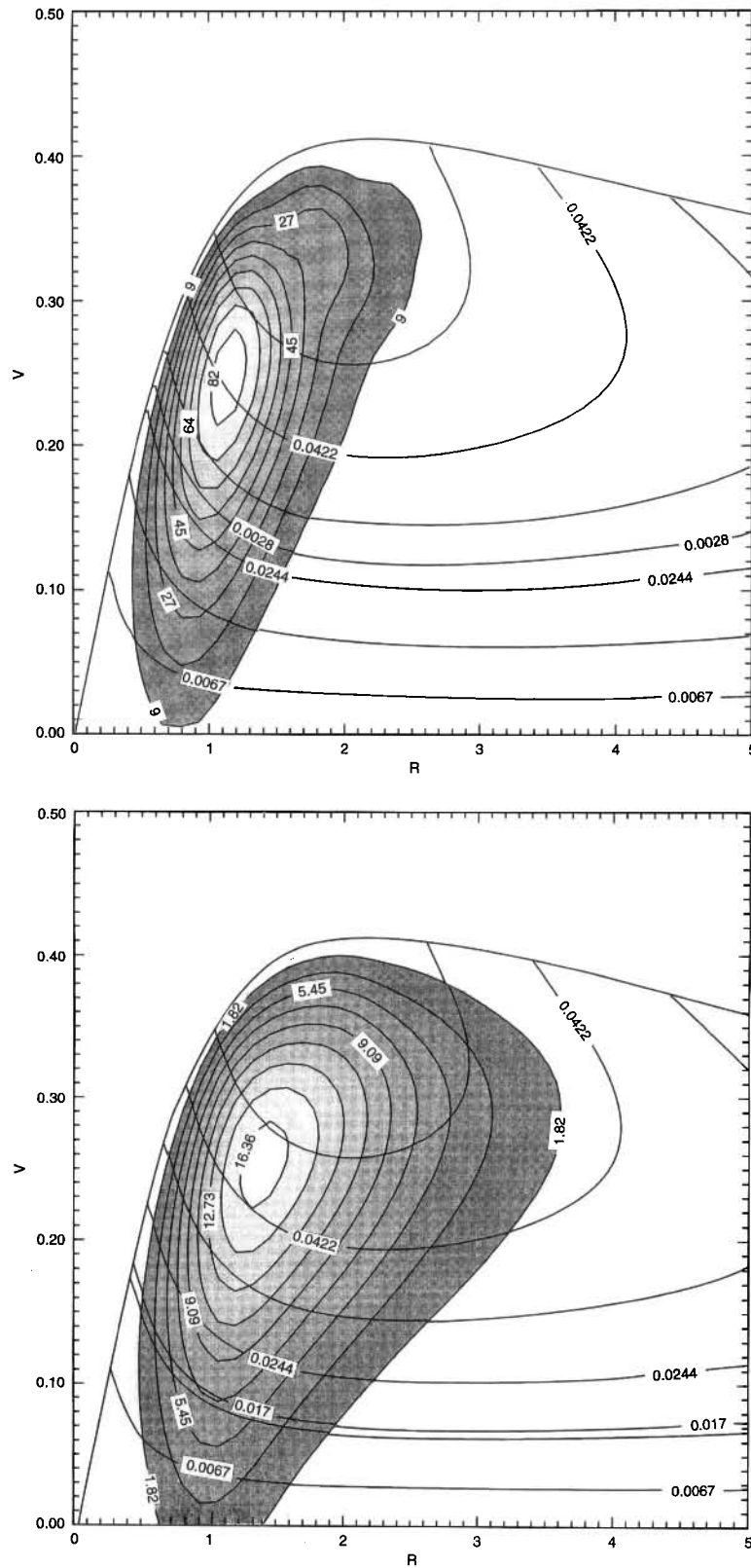
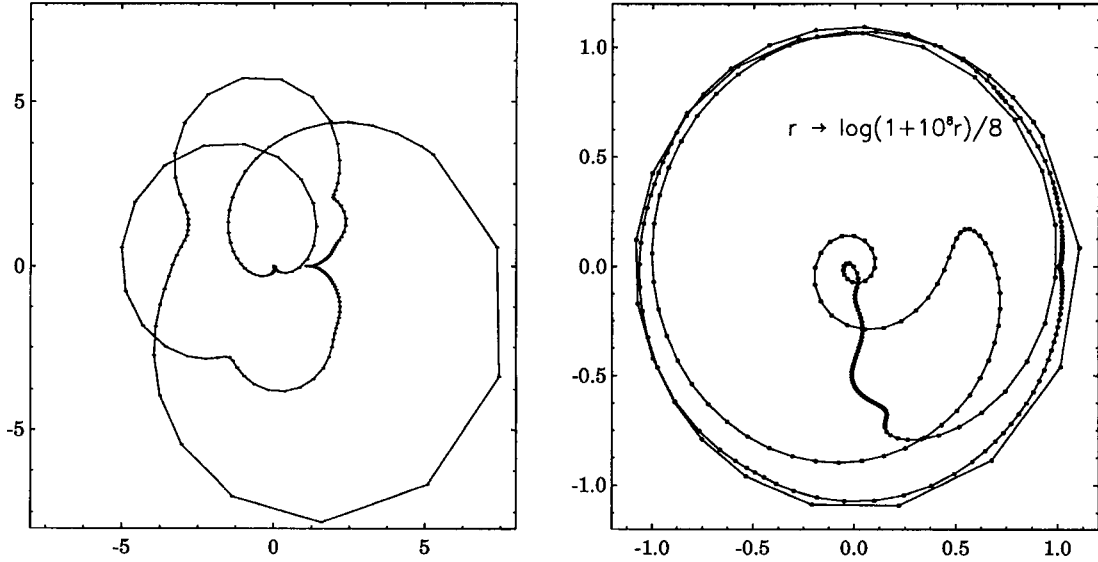
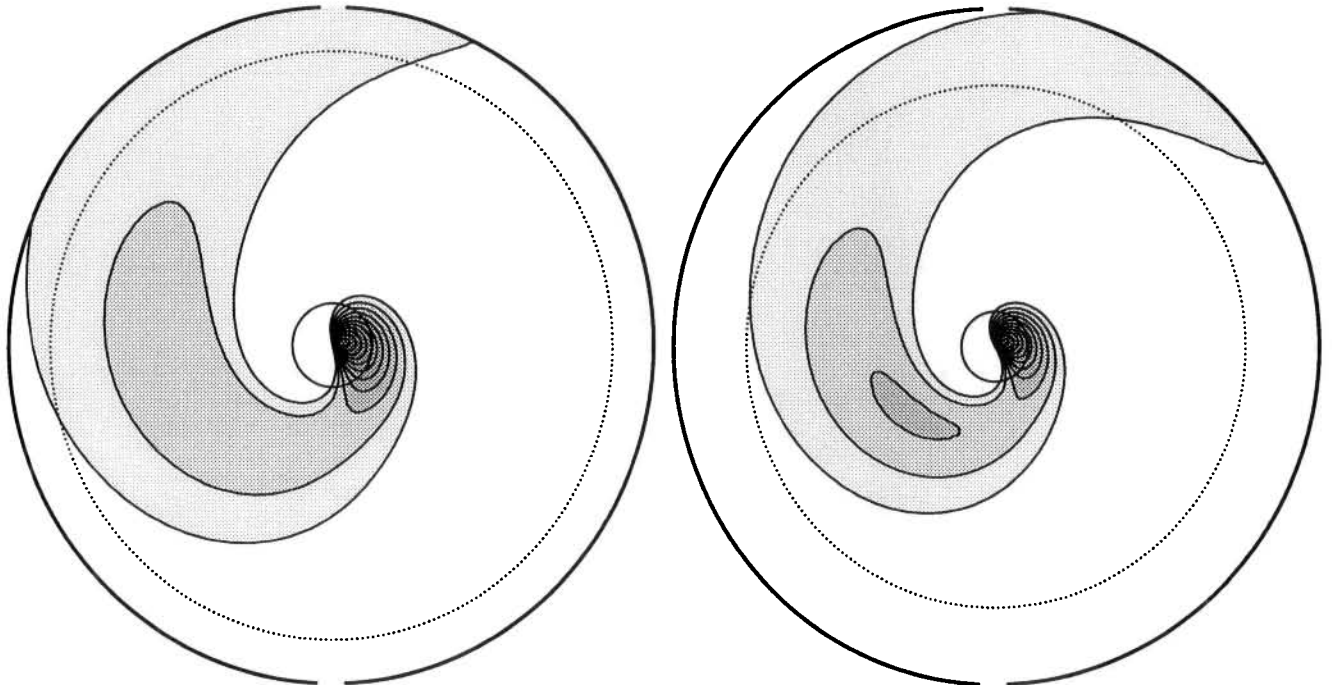


Figure 13. The orbital response in action space corresponding to the fastest growing mode described in Fig. 4. The amplitude of the left-hand side of equation (2.5) is plotted for the $\ell = -1$ (ILR) fastest growing mode of an isochrone/12 model (left-hand panel), and an isochrone/6 model (right-hand panel). Superimposed are the isocontours of the corresponding resonance $\Omega - \kappa/2$. The dashed line corresponds to the isocontour of a tenth of the pattern of the wave. Note that the hotter disc forms a Grand Design structure involving more eccentric orbits.

Table 5. First and second growth rates and pattern speeds of the $m=1$ isochrone/ m_K model.The isochrone/ m_K model: lopsided mode

Model	Pattern speed	Growth rate
9	0.135	0.0325
10	0.17	0.065
11	0.20	0.095
12	0.23	0.125

**Figure 14.** Nyquist diagram for the second $m=1$ modes of an isochrone/12 disc. There are more large loops than are seen for the bisymmetric modes, and also more structure at small scales: in the right-hand panel, the origin is shown enlarged under the mapping $r \rightarrow (1 + 10^8 r)/8$. All the space within the innermost of the three large concentric loops corresponds to the tiny cusp at the centre of the left-hand panel.**Figure 15.** The $m=1$ density response corresponding to the growing mode of the isochrone/10 and isochrone/11 model. The lopsided mode, which has a smaller growth rate, has a much more centrally concentrated response than its bisymmetric counterpart.

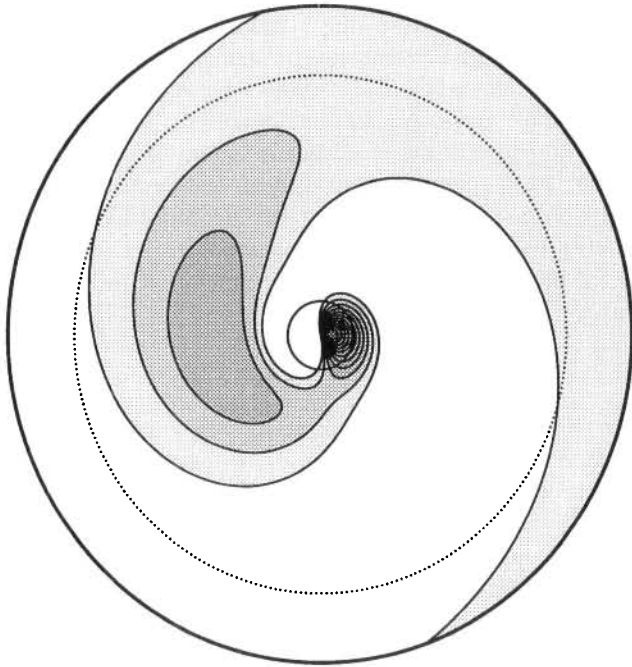


Figure 16. The $m=1$ density response corresponding to the second faster growing mode ($\Omega_p + i\eta = 0.18 + i0.075$) of the isochrone/12 model. The number of radial nodes in the response has increased by one compared to the corresponding faster mode illustrated on Fig. 15 for an isochrone/11 disc.

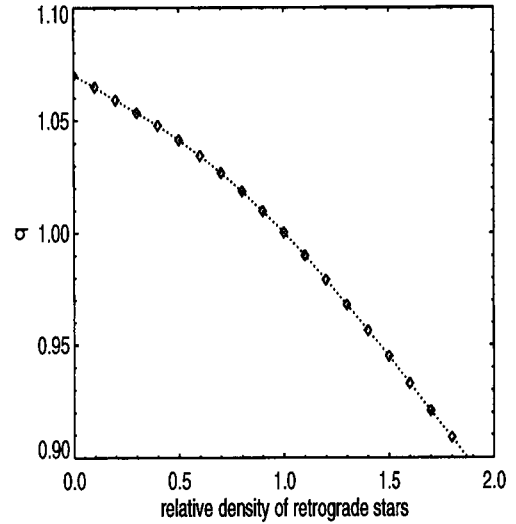


Figure 17. The effect on q of artificially modifying the density of retrograde stars in Kalnajs' isochrone/9 distribution function. The retrograde part of the distribution function has been multiplied by the factor on the ordinate, keeping the prograde stars the same. Although in Kalnajs' model stars on retrograde orbits only account for a few per cent of the total mass, they play a significant role in stabilizing the disc.

in Table 5. These modes have smaller growth rates than their bisymmetric counterparts, and are practically more difficult to isolate because they are close to other modes which grow almost as fast; the Nyquist diagrams show many large loops, all of which must be properly sampled to avoid spurious contours encircling the origin, as illustrated in Fig. 14. Indeed, when investigating weaker and weaker modes, the amount of looping in the corresponding Nyquist diagrams should increase, since modes always occur in pairs ($\omega \pm \eta$), so that when η is small, one is always in a regime corresponding to at least two (a growing and a decaying) modes.

The physical mechanism leading to the appearance of these modes needs to be clarified, but presents little practical interest when their growth rates do not correspond to the fastest growing mode. The detailed analysis of $m=1$ modes for the isochrone disc is therefore delayed until models of distribution functions which display weaker $m=2$ modes are designed.

4.3 Application to observed discs

The procedure described in Section 3 makes no assumption on the nature of the distribution function or the potential of the disc. In particular, it is well adapted to distribution functions recovered from measured discs, where the radial derivative of the potential follows from H I rotation curve of the disc, while the distribution function itself is inverted from line-of-sight velocity profiles. The technique was tested on tables generated from equation (4.5). The agreement between the 'theoretical' and 'measured' (i.e., derived from a discretized representation of the distribution) growth rates was found to be in better than 1 per cent. One peculiarity in this context lies in the finite difference chosen in the numerical derivatives of the distribution function with respect to J and h . While applying this analysis to observed data, special care should be taken in handling measurements relative to the core of the galaxy, since the relative fraction of counter-rotating stars plays a crucial role in determining the growth rates of the disc, as pointed out already by Kalnajs and illustrated in Fig. 17. This appears clearly when recalling that counter-rotating stars add up to an effective azimuthal pressure in the inner core, which therefore prevents the self-gravity of the disc to build up by orbit alignment. A non-parametric inversion technique has been devised by Pichon & Thiébaud (1997) to recover the best distribution accounting for all the measured kinematics while handling specifically the counter-rotating stars.

5 CONCLUSION AND PROSPECTS

A numerical investigation of linear stability of round galactic discs has proven successful in recovering known growth rates for the isochrone disc and the Kuzmin–Toomre discs. The method is fast and versatile, and can be applied to realistic discs with

arbitrary density and velocity profiles, and relative 'halo' support. Unstable bisymmetric growing modes for *new* equilibria, and the fastest growing lopsided modes for Kalnajs' distribution function have also been isolated to demonstrate the code's versatility. The authors are currently applying the method in a study of the stability to families of discs parametrized by their relative temperature, compactness, fraction of counter-rotating stars and halo support in order to identify the orbits responsible for the instability, and to probe the intrinsic (orbital or wave-like) nature of the $m=2$ bar instability. The nature of lopsided $m=1$ instabilities in disc galaxies is also under investigation. The implementation of linear stability analysis for observed galactic disc, yielding a direct relationship between the growth rate of the instability, the measured kinematical characteristics of the disc and the relative mass in the halo, is also being investigated. The requirement of marginal stability will provide an estimate of the minimum halo mass. All ingredients will then be in place to probe the amount of dark matter required to stabilize observed galactic discs.

ACKNOWLEDGMENTS

CP thanks J. Collett, D. Lynden-Bell, S. Tremaine, J. F. Sygnet and O. Gerhard for useful conversations. Many thanks are due to the referee, J. Sellwood, for positive criticism, to J. Binney for reading the manuscript, and to P. Englemaier for his help with **sm**. Funding from the Swiss NF and computer resources from the LAP are gratefully acknowledged.

REFERENCES

- Athanassoula E., Sellwood J., 1985, MNRAS, 221, 213
 Bertin G., 1994, ApJ, 434, 94
 Collett J., 1995, PhD thesis, Univ. Cambridge
 Earn D., Sellwood J., 1995, ApJ, 451, 533
 Hénon M., 1960, Ann. d'Astrophys., 23, 668
 Hohl F., 1971, ApJ, 168, 343
 Hunter C., 1993, in Dermott S. F., Hunter J. H., Wilson R. E., eds, Astrophysical Disks. New York Academy of Sciences
 Kalnajs A., 1971, ApJ, 166, 275
 Kalnajs A., 1976, ApJ, 205, 745
 Kalnajs A., 1977, ApJ, 212, 637
 Kalnajs A., 1978, in Berkhuisjen E., Wielebinski R., eds, Proc. IAU Symp. 77, Structures and Properties of Nearby Galaxies. Reidel, Dordrecht, p. 113
 Kuzmin G. G., 1956, Astron Zh., 33, 27
 Lynden-Bell D., 1979, MNRAS, 187, 101
 Lynden-Bell D., 1994, in Contopoulos G., Spyrou N. K., Vlahos L., eds, Galactic Dynamics and N-body Simulations: lectures at the EADN Astrophysical School, Thessaloniki. Springer-Verlag, Berlin, p. 3
 Lynden-Bell D., Kalnajs A., 1972, MNRAS, 157, 1
 Lynden-Bell D., Ostriker J., 1967, MNRAS, 136, 293
 Miyamoto, 1974, A&A, 30, 441
 Pichon C., Lynden-Bell D., 1992, Orbital instabilities in galaxies, contribution to the Ecole de Physique des Houches on: Transport Phenomena in Astrophysics, Plasma Physics and Nuclear Physics
 Pichon C., Lynden-Bell D., 1996, MNRAS, 282, 1143
 Pichon C., Thiébaud E., 1997, MNRAS, submitted
 Qian E., 1992, MNRAS, 257, 581
 Sellwood J., Wilkinson A., 1993, Rep. Prog. Phys., 56, 173
 Sygnet J. F., Kandrups H. E., 1984, ApJ, 276, 737
 Vauterin P., Dejonghe H., 1996, A&A, 313, 465
 Weinberg M. D., 1991, ApJ, 368, 66
 Zang T., 1976, PhD thesis, MIT